

A Weighted Hankel Approach and Cramér-Rao Bound Analysis for Quantitative Acoustic Microscopy Imaging

Lorena Leon, *Member, IEEE*, Jonathan Mamou, *Senior Member, IEEE*, Denis Kouamé, *Senior Member, IEEE*, and Adrian Basarab, *Senior Member, IEEE*

Abstract—Quantitative acoustic microscopy (QAM) is a cutting-edge imaging modality that leverages very high-frequency ultrasound to characterize the acoustic and mechanical properties of biological tissues at microscopic resolutions. Radio-frequency echo signals are digitized and processed to yield two-dimensional maps. This paper introduces a weighted Hankel-based spectral method with a reweighting strategy to enhance robustness with regard to noise and reduce unreliable acoustic parameter estimates. Additionally, we derive, for the first time in QAM, Cramér-Rao bounds to establish theoretical performance benchmarks for acoustic parameter estimation. Simulations and experimental results demonstrate that the proposed method consistently outperform standard autoregressive approach, particularly under challenging conditions. These advancements promise to improve the accuracy and reliability of tissue characterization, enhancing the potential of QAM for biomedical applications.

Index Terms—Quantitative acoustic microscopy, Hankel spectral method, Cramér-Rao bound, biomedical imaging

I. INTRODUCTION

QUANTITATIVE acoustic microscopy (QAM) employs ultrasound waves with frequencies exceeding 100 MHz to scan thin (5-14 μm thick) *ex vivo* tissue sections affixed to microscopy slides, using filtered water as the coupling medium [1]. This advanced imaging technique generates two-dimensional (2D) maps of acoustic properties, including speed of sound, impedance, and acoustic attenuation, in addition to mechanical properties such as bulk modulus, density, and compressibility, achieving spatial resolutions near the acoustic wavelength (e.g., finer than 8 μm at 250 MHz [2]). QAM offers unique and complementary advantages compared to conventional microscopy modalities (e.g., optical microscopy, electron microscopy, and histological imaging) for detailed tissue characterization [3]. Its versatility has been demonstrated in a wide range of applications, including corneal imaging [4],

retinal studies [5], [6], liver tissue analysis [7], cerebellar folding [8], biomechanical changes in myopic eyes [9], [10], cancerous lymph nodes investigations [11], and living cells analysis [3], [12], [13].

Data acquired by QAM instruments consist of radio frequency (RF) signals containing two main reflections originating from the water-sample and sample-glass interfaces. These RF signals are then processed offline using model-based approaches to estimate acoustic parameters at each scanned position. While time-domain methods [12] have been explored, frequency-domain techniques have proven advantageous, particularly when reflections overlap in time [14]. The state-of-the-art in QAM, introduced by Rohrbach et al. [15], employs an autoregressive (AR) frequency-domain model with a spectral estimation algorithm inspired by the classical Prony method [16] and the annihilating filter [17].

Despite the advantages of the AR-based method, QAM continues to face challenges in decomposing signals into primary reflection components and obtaining reliable estimates. These challenges become particularly critical when dealing with high noise levels, thin tissue samples (i.e., \sim acoustic wavelength), small impedance contrast, or large tissue attenuation. These difficulties limit the full potential of QAM for high-resolution tissue characterization.

The goal of this work is to propose a robust spectral-based QAM framework to address the aforementioned limitations in acoustic parameter estimation. To that end, the QAM measurement forward model and image formation process are briefly recalled in Section II.

The first contribution, presented in Section III, is the introduction of a weighted Hankel-based method that builds on Hankel matrix theory, as inspired by [18], to address the spectral estimation problem. In contrast to our previous approach [19], an iterative reweighting strategy is incorporated, to further improve robustness by mitigating the influence of outliers in the spectral data and minimize unreliable acoustic parameter estimates.

The second contribution, detailed in Section IV, is the derivation of the Cramér-Rao bounds presented for the first time in the context of QAM. These bounds establish theoretical performance benchmarks for evaluating and comparing the different estimators.

The third contribution is the rigorous evaluation of the

This work was supported by NIH grant R01GM143388 (JM).

L. Leon and A. Basarab are with Univ Lyon, Université Claude Bernard Lyon 1, CNRS, Inserm, CREATIS UMR 5220, U1294, France (e-mail: lorena.leon@creatis.insa-lyon.fr; adrian.basarab@creatis.insa-lyon.fr).

J. Mamou is with Weill Cornell Medicine College, Department of Radiology, New York, NY, USA (e-mail: jom4032@med.cornell.edu).

D. Kouamé is with IRIT, University of Toulouse, CNRS 5505, Université Paul Sabatier Toulouse 3, France (e-mail: denis.kouame@irit.fr).

proposed methods against the standard AR model through simulations and experimental data obtained from soft tissues using a QAM instrument operating at 500 MHz, as detailed in Section V. The performance results, presented in Section VI, demonstrate that the proposed methodology achieves a significant reduction in unreliable estimates and improved estimation accuracy, all while incurring only a moderate additional computational cost. Finally, Section VII discusses the findings and outlines potential directions for future research.

II. SIGNAL MODEL IN QAM

In QAM, an RF signal acquired in a tissue-free location results from a single reflection from the glass-water interface and serves as a reference signal, denoted by $h_0(t)$, where t is the time (in seconds). On the other hand, a signal acquired at a tissue location, denoted by $h(t)$, is composed of two main reflections: one from the water-tissue interface ($h_1(t)$) and the other from the tissue-glass interface ($h_2(t)$). Fig. 1 illustrates the measurement principle in a tissue location (i.e., h_1 and h_2) and a tissue-free location (i.e., h_0).

In this context, the estimation of the acoustic properties of the sample relies on the accurate identification and characterization of h_1 and h_2 in terms of their amplitude, frequency attenuation, and time shift relative to h_0 . This section provides an overview of the signal model, the estimation problem, and the image formation process involved in QAM technology.

A. From time to frequency domain

To account for the complex interactions of the acoustic waves within the tissue, including potential scattering effects and multiple reflections, we consider

$$h(t) = \sum_{p=1}^P h_p(t) \text{ with } P \geq 2, \quad (1)$$

where P , known as the model order, represents the number of reflections present in the acquired signal [15]. At this stage, we assume P to be given, and the choice of its value is discussed in Section V-D.

Each echo h_p in (1) can be modeled as a phase-shifted and amplitude-modified version of the reference signal h_0 , i.e.,

$$h_p(t) = A_p h_0^{\beta_p}(t - t_p), \quad (2)$$

where A_p is the amplitude, t_p is the time of flight (TOF) and β_p symbolizes an additional frequency-dependent attenuation effect due to the round-trip propagation inside the sample.

Parameter estimation based on (1)-(2) becomes particularly challenging when echo signals overlap in time, as this complicates their separation. Furthermore, identifying the tissue-glass reflection becomes problematic when the sample is very thin or its impedance is close to that of the water used as a coupling medium. To overcome these challenges, the transition to the frequency domain has proven to be an effective approach [15].

Let \mathcal{F}_{h_0} and \mathcal{F}_h denote the discrete Fourier transform (DFT) of the digital version of h_0 and h , respectively. The ratio

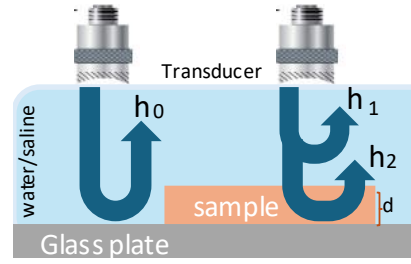


Fig. 1. Diagram of the experimental QAM approach. The measured signal h comprises two components: h_1 and h_2 , corresponding to reflections from the water-tissue and tissue-glass interfaces, respectively. The reference signal h_0 results from a single reflection at the glass-water interface in a tissue-free location.

between these two transforms at discrete frequencies $k\Delta f$ can be written as [15]

$$\frac{\mathcal{F}_h(k\Delta f)}{\mathcal{F}_{h_0}(k\Delta f)} = \sum_{p=1}^P A_p [\exp(2\pi\Delta f[-\beta_p - i\Delta t_p])]^k, \quad (3)$$

where $\Delta f = f_s/(2M)$ denotes the frequency step size, M represents the number of temporal samples (considering no zero-padding), and f_s is the sampling frequency. In (3), the attenuation coefficient β_p describes how the amplitude of the signal decreases with frequency, and the relative time shift of the p th echo compared to the reference signal is given by $\Delta t_p = t_p - t_0$.

The normalization (i.e., division) in (3) is well-defined where \mathcal{F}_{h_0} is non-zero, which is guaranteed for frequencies within the bandwidth of the transducer where sufficiently high signal-to-noise ratio can be achieved. At this stage, we assume the bandwidth is known, with k_{\min} and k_{\max} defining the frequency limits as $k_{\min}\Delta f$ and $k_{\max}\Delta f$, respectively. For simplicity, we assume $k_{\max} - k_{\min} = 2N$, resulting in a total of $2N + 1$ frequencies. The choice of bandwidth is further discussed in Section V-D.

A noisy observation of the spectrum defined in (3) can be seen as a special case of the following general parametric model

$$x_\kappa = \sum_{p=1}^P a_p \lambda_p^\kappa + \epsilon_\kappa, \quad (4)$$

with $\lambda_p = \exp(2\pi(\gamma_p + i\nu_p))$, where γ_p and ν_p are the damping and the frequency parameters; and ϵ_κ is a complex additive noise. Furthermore, $a_p = A_p \exp(ib_p)$ represents the complex-valued amplitude, where $A_p = |a_p|$ is the real-valued amplitude, and $b_p = \angle a_p$ is the initial phase. By defining $\kappa = k/(2M)$, a noisy observation of (3) and model (4) are equivalent if $b_p = 0$, $\gamma_p = -\beta_p f_s$, $\nu_p = -\Delta t_p f_s$ for all $p = 1, \dots, P$.

The model (4) arises in various applications, such as astronomy, radar, communications, economics, medical imaging, and spectroscopy, to name but a few (see, e.g., [20] and the references therein). Unlike [15] and [19], this work opts to present the spectral model in its general form (4) instead of (3) to facilitate the derivation of the theoretical bounds in Section IV.

B. Acoustic parameter estimation and image formation

Given $\{\lambda_p\}_{p=1}^P$ and $\{a_p\}_{p=1}^P$, the two leading reflections can be determined by reconstructing the P pulses and computing the amplitude of the maximum of the Hilbert-transformed signals. The two pulses with the largest amplitudes correspond to the desired components related to the water-tissue and tissue-glass interfaces, which are denoted with the subscripts $p=1$ and $p=2$, without loss of generality. Then, the signal corresponding to water-sample interface is identified as the one with the smallest TOF ($t_1 < t_2$), as it occurs before the sample-glass interface.

Following the derivations in [15] and using the parameter notation from (4), the speed of sound c (in m/s) and the acoustic impedance Z (in MRayl) can be computed as

$$c = c_w \frac{\nu_1}{\nu_1 - \nu_2}, \quad Z = Z_w \frac{1 + \frac{A_1}{R_{wg}}}{1 - \frac{A_1}{R_{wg}}}, \quad (5)$$

where c_w and Z_w are the known speed of sound and acoustic impedance in the water, and R_{wg} is the known pressure reflection coefficient between water and glass.

The tissue attenuation $\alpha = \beta_2/(2d)$ (in dB/MHz/cm) quantifies the signal attenuation during its round-trip travel through tissue with a thickness d (in μm). Their values are obtained as follows,

$$d = \frac{c_w \nu_1}{2 f_s}, \quad \alpha = -\frac{\gamma_2}{c_w \nu_1}. \quad (6)$$

It is important to note that a linear attenuation model is assumed to be valid within the specified bandwidth; for a nonlinear attenuation model, refer to [15].

Finally, a 2D map of each acoustic tissue property is obtained by combining the estimates obtained by applying the parameter-estimation algorithm to all scanned locations.

III. WEIGHTED HANKEL-BASED PARAMETER ESTIMATION

The accurate estimation of c , Z , α , and d fundamentally depends on the precise determination of the spectral parameters (λ_1, a_1) and (λ_2, a_2) . Although recovering amplitudes a_p can be efficiently addressed using a least-squares (LS) approach, the primary challenge lies in accurately estimating λ_p .

To overcome the limitations of the standard AR-based framework for QAM [15], we previously introduced a Hankel (HK)-based spectral estimation framework for QAM image formation [19]. This method builds upon the HK spectral estimation technique originally presented in [18]. In this work, we extend our previous approach and propose a weighted HK-based method that incorporates a reweighting strategy, designed to better handle noisy data points within the normalized spectrum (i.e., (3)).

A. HK-based problem formulation

The HK spectral method applies to the parametric model (4) and seeks to approximate the vector $\mathbf{x} = (x_{\kappa_1}, \dots, x_{\kappa_{2N+1}})$ by another vector $\mathbf{g} = (g_{\kappa_1}, \dots, g_{\kappa_{2N+1}})$, whose elements are expressed as a linear combination of complex exponentials

$$g_{\kappa_n} = \sum_{p=1}^P a_p \lambda_p^{\kappa_n}. \quad (7)$$

with $n = 1, 2, \dots, 2N + 1$.

A Hankel matrix $\mathbf{H} = H(\mathbf{g})$, generated element-wise from a vector \mathbf{g} , is a symmetric matrix where each ascending skew diagonal from left to right is constant such that $[\mathbf{H}]_{ij} = g_{\kappa_{i+j-1}}$ with $1 \leq i, j \leq N + 1$.

Kronecker's theorem [21], [22] for complex symmetric matrices establishes that $\text{rank}(\mathbf{H}) = P$ if and only if there exist $\{\lambda_p\}_{p=1}^P$ and $\{a_p\}_{p=1}^P$ in \mathbb{C} such that $g_{\kappa} = \sum_{p=1}^P a_p \lambda_p^{\kappa}$ for equally spaced indices $\kappa = \kappa_1, \dots, \kappa_{2N+1}$.

Consequently, the best approximation (in the l_2 -norm sense) of \mathbf{x} by a linear combination of P complex exponentials is given by the vector \mathbf{g} which satisfies $\text{rank}(H(\mathbf{g})) = P$ and minimizes the l_2 -norm of the difference $\mathbf{x} - \mathbf{g}$. Inspired by [18], \mathbf{g} is obtained as the solution of the optimization problem

$$\begin{aligned} & \underset{\mathbf{A}, \mathbf{g}}{\text{minimize}} \quad \frac{1}{2} \mathbf{w}^T \|\mathbf{x} - \mathbf{g}\|_2^2 + \mathcal{R}_P(\mathbf{H}), \\ & \text{subject to} \quad \mathbf{H} = H(\mathbf{g}), \end{aligned} \quad (8)$$

where $\mathcal{R}_P(\mathbf{H})$ is an indicator function for square matrices, defined as $\mathcal{R}_P(\mathbf{H}) = 0$ if $\text{rank}(\mathbf{H}) \leq P$ and infinity otherwise, and $\|\cdot\|_2$ stands for l_2 vector norm. The weight vector $\mathbf{w} = (w_{\kappa_1}, \dots, w_{\kappa_{2N+1}})$ can be chosen depending on the specific application. In Section III-D, we propose an iteratively reweighted approach to mitigate data noise.

B. ADMM-based solution

The optimization problem (8) can be solved using the alternating direction method of multipliers (ADMM) method [23], an iterative technique where a solution to a large global problem is obtained by solving smaller sub-problems. To solve (8), the ADMM algorithm transitions from iteration q to iteration $q + 1$ as follows

$$\mathbf{H}^{q+1} = \underset{\mathbf{H}}{\text{argmin}} \mathcal{L}(\mathbf{H}, \mathbf{g}^q, \mathbf{\Lambda}^q), \quad (9)$$

$$\mathbf{g}^{q+1} = \underset{\mathbf{g}}{\text{argmin}} \mathcal{L}(\mathbf{H}^{q+1}, \mathbf{g}, \mathbf{\Lambda}^q), \quad (10)$$

$$\mathbf{\Lambda}^{q+1} = \mathbf{\Lambda}^q + \rho(\mathbf{H}^{q+1} - H(\mathbf{g}^{q+1})), \quad (11)$$

where $\mathbf{\Lambda}$ is the Lagrange multiplier matrix, and

$$\begin{aligned} \mathcal{L}(\mathbf{H}, \mathbf{g}, \mathbf{\Lambda}) = & \mathcal{R}_P(\mathbf{H}) + \frac{1}{2} \mathbf{w}^T \|\mathbf{x} - \mathbf{g}\|_2^2 \\ & + \langle \mathbf{\Lambda}, \mathbf{H} - H(\mathbf{g}) \rangle_{\text{Re}} + \frac{\rho}{2} \|\mathbf{H} - H(\mathbf{g})\|_F^2, \end{aligned} \quad (12)$$

is the augmented Lagrangian associated with (8). In (12), ρ is a penalty coefficient, $\langle \mathbf{A}, \mathbf{B} \rangle_{\text{Re}} = \text{real}(\text{tr}(\mathbf{A}\mathbf{B}^H))$ denotes the inner product between the matrices \mathbf{A} and \mathbf{B} , \cdot^H is the conjugate transpose, and $\|\mathbf{A}\|_F^2 = \langle \mathbf{A}, \mathbf{A} \rangle_{\text{Re}}$ is the Frobenius norm.

The ADMM procedure defined in (9)-(10)-(11) ends after a finite number Q of iterations. The rank constraint makes (8) a non-convex problem, meaning that convergence to a unique solution is not guaranteed and may depend on the choice of parameters ρ and Q as well as the initial values \mathbf{g}^0 and $\mathbf{\Lambda}^0$. Nevertheless, results in [18] show that the HK-based spectral

method performs substantially better than established high-resolution techniques like ESPRIT [24]. In this work, we fixed the parameters to $Q = 200$, $\rho = 0.025$, $\mathbf{g}^0 = \mathbf{x}$ and $\mathbf{\Lambda}^0 = \mathbf{0}$, following the configuration in [18], [19].

The most computationally intensive operation in each iteration step q is the singular value decomposition (SVD) performed during the update of \mathbf{H} . The time complexity of the SVD operation is $\mathcal{O}(N^3)$, leading to an overall time complexity for the algorithm of $\mathcal{O}(QN^3)$. In comparison, the ESPRIT method requires the computation of only a single SVD, while the AR approach does not require any SVD computations.

Due to the regularization term $\frac{\rho}{2} \|\mathbf{H} - H(\mathbf{g})\|_F^2$ in (12), it is common that $\hat{\mathbf{H}} \neq H(\hat{\mathbf{g}})$, where $\hat{\mathbf{H}}$ and $\hat{\mathbf{g}}$ are estimates of \mathbf{H} and \mathbf{g} resulting from the ADMM algorithm. This discrepancy suggests that $\hat{\mathbf{g}}$ or the vector $\hat{\mathbf{x}}^{\text{approx}}$, obtained by averaging the anti-diagonals terms of $\hat{\mathbf{H}}$ provides a valid approximation of a sum of exponential functions and can serve as a solution to (8). The vector $\hat{\mathbf{x}}^{\text{approx}}$ is defined element-wise as

$$x_{\kappa_n}^{\text{approx}} = \frac{1}{\mu_n} \sum_{i+j=n+1} [\hat{\mathbf{H}}]_{ij}, \quad (13)$$

where μ_n is the number of times that $\hat{\mathbf{g}}_{\kappa_n}$ appears in the matrix $\hat{\mathbf{H}}$. Finally, the latter $\mathbf{x}^{\text{approx}}$ is considered a more appropriate solution because $\hat{\mathbf{g}}$ is computed to best approximate the noisy data.

C. Spectral parameter estimation

By construction, the Hankel matrix solution $\mathbf{H} = H(\mathbf{x}^{\text{approx}})$ is a complex symmetric matrix which satisfies $\mathbf{H} = \mathbf{H}^T$ and $\text{rank}(\mathbf{H}) = P$. For matrices with these properties, one can choose the matrices \mathbf{U} and \mathbf{V} appearing in the SVD of \mathbf{H} , i.e., $\mathbf{H} = \mathbf{U}\mathbf{\Sigma}\mathbf{V}^H$ such that $\mathbf{U} = \overline{\mathbf{V}}$, where the bar indicates complex conjugation. Consequently,

$$\mathbf{H} = \sum_{p=1}^P s_p \mathbf{u}_p \mathbf{u}_p^T, \quad s_p \in \mathbb{R}^+, \quad \mathbf{u}_p \in \mathbb{C}^{2N+1} \quad (14)$$

where $s_1, s_2, \dots, s_P > 0$ are the eigenvalues of \mathbf{H} . Moreover, the con-eigenvectors \mathbf{u}_p are orthogonal, satisfy the relation $\mathbf{H}\bar{\mathbf{u}}_p = s_p \mathbf{u}_p$ and can be expressed as the sum of the same P exponentials of $\mathbf{x}^{\text{approx}}$.

Hence, we can decompose the matrix $\mathbf{U} = (\mathbf{u}_1, \dots, \mathbf{u}_P)$ as $\mathbf{U} = \mathbf{E}\mathbf{G}$, where \mathbf{G} is some invertible $P \times P$ matrix and \mathbf{E} is a $2N+1 \times P$ Vandermonde-like matrix defined by $[\mathbf{E}]_{np} = \lambda_p^{\kappa_n}$, for $p=1, \dots, P$ and $n=1, \dots, 2N+1$, i.e.,

$$\mathbf{E} = \begin{pmatrix} \lambda_1^{\kappa_1} & \dots & \lambda_P^{\kappa_1} \\ \vdots & \ddots & \vdots \\ \lambda_1^{\kappa_{2N+1}} & \dots & \lambda_P^{\kappa_{2N+1}} \end{pmatrix}. \quad (15)$$

Let \mathbf{U}^f (resp. \mathbf{U}^l) denote the matrix \mathbf{U} whose first row (resp. last row) has been dropped. Since $\mathbf{U}^f = \mathbf{E}^f \mathbf{G}$, $\mathbf{U}^l = \mathbf{E}^l \mathbf{G}$ and given the structure of \mathbf{E} , it is possible to obtain $\mathbf{E}^f = \text{diag}(\lambda_1, \dots, \lambda_P) \mathbf{E}^l$. Consequently,

$$(\mathbf{U}^l)^\dagger \mathbf{U}^f = \mathbf{G}^{-1} \text{diag}(\lambda_1, \dots, \lambda_P) \mathbf{G}$$

where \cdot^\dagger denotes the pseudo-inverse operator. Therefore, $\{\lambda_p\}_{p=1}^P$ can be obtained by computing the eigenvalues of $(\mathbf{U}^l)^\dagger \mathbf{U}^f$.

Finally, the amplitudes $\{a_p\}_{p=1}^P$ are estimated using the LS estimator

$$\hat{\mathbf{a}} = (\mathbf{E}^T \mathbf{E})^{-1} (\mathbf{E} \mathbf{x}), \quad (16)$$

where $\hat{\mathbf{a}} = (\hat{a}_1, \hat{a}_2, \dots, \hat{a}_P)$.

D. Iteratively re-weighted approach

We propose to use a weight function based on redescending M-estimators to reduce the impact of noisy data points on estimates. Specifically, we adopt the Tukey bisquare weight function [25], [26], which robustly rejects outliers, defined as

$$w_\kappa = \begin{cases} (1 - (e_\kappa / (c\delta))^2)^2 & \text{if } |e_\kappa| \leq c\delta, \\ 0 & \text{otherwise,} \end{cases} \quad (17)$$

where e_κ is the residual error at the data point κ and $c > 0$ is a constant fixed a priori. The scale parameter $\delta > 0$ represents the standard deviation of the residual errors for the inlier estimates, and is generally estimated using a robust estimator such as the median absolute deviation (MAD) [27]

$$\hat{\delta}_{\text{MAD}} = \delta_0 \text{median}_{n=1, \dots, 2N+1} (|e_{\kappa_n} - \text{median}(e)|)$$

with $e = (e_{\kappa_1}, \dots, e_{\kappa_{2N+1}})$ and $\delta_0 = 1.4826$ is a scaling constant for Gaussian errors [28].

The proposed iteratively reweighting strategy starts with initial weights set to 1 (no weighting). After performing spectral estimation, the residuals from the spectral reconstruction are calculated, and the weights are updated according to (17). This iterative process gradually down-weights outliers (data points with high residuals), thereby reducing their influence on the estimation and improving robustness in the presence of noise.

Our experiments indicate that repeating this process three times provides a good balance between computational efficiency and estimation accuracy.

IV. CRAMÉR-RAO BOUNDS

The Cramér-Rao bound (CRB) [29] is a theoretical lower bound on the variance of any unbiased estimator for a given parametric model. The CRB provides a valuable benchmark for assessing the performance of estimation algorithms, as it defines the best achievable performance given the statistical characteristics of the data and the noise. In addition, deriving this bound offers insight into the estimation problem by identifying which parameters are more difficult to estimate and under what conditions. It also helps corroborate the underlying physical theory and establish experimental conditions that enable accurate parameter estimation.

In this section, we derive the CRB for the estimation of the acoustic parameters within the framework established in Section II. First, we present the CRB for the spectral parameters of the model defined in (4). Then, leveraging the functional invariance property, we derive the CRB for the acoustic parameters of interest. This final derivation represents a key contribution of this work.

A. Bounds for spectral parameter estimation

The CRB for the real-valued parameter vector $\boldsymbol{\theta} = (A_1, \dots, A_P, b_1, \dots, b_P, \gamma_1, \dots, \gamma_P, \nu_1, \dots, \nu_P)$ in spectral model (4) is defined by the diagonal elements of the inverse of the Fisher Information Matrix (FIM) $\mathbf{F}(\boldsymbol{\theta})$ [29], i.e.,

$$\text{CRB}(\boldsymbol{\theta}_i) = [\mathbf{F}^{-1}(\boldsymbol{\theta})]_{ii}. \quad (18)$$

We assume that the error ϵ_κ in (4) is zero mean, uncorrelated, and follows a complex Gaussian distribution, with independent real and imaginary components, each having variance $\sigma^2/2$. Under these conditions, the FIM can be computed using the Slepian-Bang's formula [20], i.e.,

$$\mathbf{F}(\boldsymbol{\theta}) = \frac{2}{\sigma^2} \text{real} \left(\left(\frac{\partial \mathbf{g}}{\partial \boldsymbol{\theta}} \right)^H \left(\frac{\partial \mathbf{g}}{\partial \boldsymbol{\theta}} \right) \right). \quad (19)$$

Following the presentations in [30] and [31], we use the derivatives $\frac{\partial g_\kappa}{\partial A_p} = \exp(ib_p)\lambda_p^\kappa$, $\frac{\partial g_\kappa}{\partial \beta_p} = ia_p\lambda_p^\kappa$, $\frac{\partial g_\kappa}{\partial \gamma_p} = 2\pi\kappa_p\lambda_p^\kappa$ and $\frac{\partial g_\kappa}{\partial \nu_p} = i2\pi\kappa_a\lambda_p^\kappa$ to form the matrix

$$\mathbf{Q} = [\mathbf{EB} \quad i\mathbf{EB} \quad 2\pi\tilde{\mathbf{E}}\mathbf{B} \quad i2\pi\tilde{\mathbf{E}}\mathbf{B}], \quad (20)$$

where \mathbf{E} is defined in (15),

$$\tilde{\mathbf{E}} = \begin{pmatrix} \kappa_1\lambda_1^{\kappa_1} & \dots & \kappa_1\lambda_P^{\kappa_1} \\ \vdots & \ddots & \vdots \\ \kappa_{2N+1}\lambda_1^{\kappa_{2N+1}} & \dots & \kappa_{2N+1}\lambda_P^{\kappa_{2N+1}} \end{pmatrix},$$

and $\mathbf{B} = \text{diag}\{(\exp(ib_1), \dots, \exp(ib_P))\}$. Therefore, we can express the inverse FIM as

$$\mathbf{F}^{-1}(\boldsymbol{\theta}) = \frac{\sigma^2}{2} \mathbf{P}^{-1} \left(\text{real} \left(\mathbf{Q}^H \mathbf{Q} \right) \right)^{-1} \mathbf{P}^{-1}, \quad (21)$$

where $\mathbf{P} = \text{diag}[\mathbf{I} \ \mathbf{A} \ \mathbf{A} \ \mathbf{A}]$ with $\mathbf{A} = \text{diag}\{(a_1, \dots, a_p)\}$.

B. Bounds for acoustic parameter estimation

As observed in (5) and (6), the acoustic parameters are determined through transformations of the spectral parameters $\boldsymbol{\theta}$. We denote these transformations as $\boldsymbol{\phi} = (\phi_1, \phi_2, \phi_3, \phi_4)$, where $\phi_1(\boldsymbol{\theta}) = c$, $\phi_2(\boldsymbol{\theta}) = d$, $\phi_3(\boldsymbol{\theta}) = \alpha$, $\phi_4(\boldsymbol{\theta}) = Z$. Using the functional invariance property of the CRB [29], we obtain the CRB for the acoustic parameters as the diagonal elements of the inverse of the transformed FIM, denoted by $\mathbf{F}_\phi^{-1}(\boldsymbol{\theta})$ and computed as

$$\mathbf{F}_\phi^{-1}(\boldsymbol{\theta}) = \nabla_\theta[\boldsymbol{\phi}^T(\boldsymbol{\theta})]^T \mathbf{F}^{-1}(\boldsymbol{\theta}) \nabla_\theta[\boldsymbol{\phi}^T(\boldsymbol{\theta})], \quad (22)$$

where $\nabla_\theta[\boldsymbol{\phi}^T(\boldsymbol{\theta})] = \left(\frac{\partial \phi_1(\boldsymbol{\theta})}{\partial \boldsymbol{\theta}}, \frac{\partial \phi_2(\boldsymbol{\theta})}{\partial \boldsymbol{\theta}}, \frac{\partial \phi_3(\boldsymbol{\theta})}{\partial \boldsymbol{\theta}}, \frac{\partial \phi_4(\boldsymbol{\theta})}{\partial \boldsymbol{\theta}} \right)$

is the Jacobian matrix of $\boldsymbol{\phi}^T(\boldsymbol{\theta})$ with respect to $\boldsymbol{\theta}$. The partial derivatives required to construct the Jacobian are given by

$$\frac{\partial \phi_1(\boldsymbol{\theta})}{\partial \boldsymbol{\theta}} = (\mathbf{0}_{3P}, c_w\nu_2/(\nu_1 - \nu_2)^2, c_w\nu_1/(\nu_1 - \nu_2)^2, \mathbf{0}_{P-2}),$$

$$\frac{\partial \phi_2(\boldsymbol{\theta})}{\partial \boldsymbol{\theta}} = (\mathbf{0}_{3P}, c_w/(2f_s), \mathbf{0}_{P-1}),$$

$$\frac{\partial \phi_3(\boldsymbol{\theta})}{\partial \boldsymbol{\theta}} = (\mathbf{0}_{2P+1}, 1/(c_w\nu_1), \mathbf{0}_{P-2}, \gamma_2/(c_w\nu_1^2), \mathbf{0}_{P-1}),$$

$$\frac{\partial \phi_4(\boldsymbol{\theta})}{\partial \boldsymbol{\theta}} = (2Z_w/(R_{wg}(1 - a_1/R_{wg})^2, \mathbf{0}_{4P-1}),$$

where $\mathbf{0}_K$ represents a vector of zeros of size K .

Finding closed-form expressions for the CRB becomes challenging due to the dense structure of the matrix \mathbf{Q} . Ultimately, we express the CRBs for the acoustic parameters as

$$\begin{aligned} \text{CRB}_c &= [\mathbf{F}_\phi^{-1}(\boldsymbol{\theta})]_{11}, & \text{CRB}_d &= [\mathbf{F}_\phi^{-1}(\boldsymbol{\theta})]_{22}, \\ \text{CRB}_\alpha &= [\mathbf{F}_\phi^{-1}(\boldsymbol{\theta})]_{33}, & \text{CRB}_Z &= [\mathbf{F}_\phi^{-1}(\boldsymbol{\theta})]_{44}. \end{aligned} \quad (23)$$

The only clear dependency that can be extracted from these formulas is that on the noise level. Specifically, all acoustic CRBs in (23) are scaled by a factor of $\sigma^2/2$ coming from (21), indicating that the CRBs increase proportionally to the noise variance. Furthermore, the acoustic CRBs explicitly depend on the spectral values and implicitly on the acoustic parameters themselves. This latter dependency is examined in the results section through simulations.

V. MATERIAL AND METHODS

Current QAM systems are capable of operating at frequencies of 250 MHz [6] and 500 MHz [32]. Although increasing the transducer frequency improves spatial resolution, it also introduces heightened sensitivity to environmental factors such as vibrations and temperature fluctuations, increasing the challenges in the estimation of acoustic parameters.

The HK-based methods introduced in Section III, referred to as RHK for the proposed reweighted approach and HK for the nonweighted variant [19] (which corresponds to the first iteration of RHK), along with the standard AR-based algorithm [15], are applicable across different transducer frequencies. In this study, we focus on real and simulated QAM data acquired using a 500 MHz transducer.

In QAM, estimates are considered outliers if they fall outside physically admissible ranges, specifically $c < 1500$ m/s, $c > 2200$ m/s, $Z < 1.48$ MRayl, or $Z > 2.2$ MRayl [15]. Therefore, beyond assessing estimator accuracy, the outlier count serves as an additional metric to evaluate the efficacy of each method.

A. Simulation setting

For a given set of acoustic parameters, we simulated QAM RF signals applying the inverse Fourier transform to the model in (3), setting $P=2$, $M=300$, and $f_s=10$ GHz. The resulting signals were then perturbed by independent and identically distributed (i.i.d.) zero mean Gaussian noise with variance σ_x^2 , given by

$$\sigma_x = 10^{(20 \log_{10}((\xi(h_0) - \text{SNR})/20))}, \quad (24)$$

where $\xi(h_0)$ is the maximum of the absolute value of the envelope of h_0 , estimated using its Hilbert transform-based analytic signal [15]. This noise formulation ensures that the simulated signals maintain the desired signal-to-noise ratio (SNR) in the time domain, representing the difference in decibels between the amplitude of the reference signal and the added noise. To assess estimation performance, we generated 200 realizations of the random Gaussian noise for each parameter configuration.

To reflect real-world conditions, we used a measured reference signal h_0 from our 500 MHz QAM system [32] and

TABLE I
SIMULATED PARAMETER VARIATIONS

Parameter	Lower value	Step size	Upper value
SNR [dB]	20	5	100
Z [MRayl]	1.51	0.01	1.63
α [dB/MHz/cm]	8	1	20
d [μm]	1	0.5	8
bandwidth [dB]	-4	-2	-20

set the acoustic parameters to experimentally relevant values for QAM applications. These values were chosen based on preliminary tests to determine the optimal range between easily separable scenarios (e.g., large SNR, d and $|Z - Z_w|$, and small α) with more challenging cases (e.g., small SNR, d , and $|Z - Z_w|$, and large α) [15].

In each simulation, we varied the parameter under investigation while keeping the remaining parameters fixed as follows: SNR = 50 dB, $d = 4 \mu\text{m}$, $Z = 1.63 \text{ MRayl}$, $c = 1600 \text{ m/s}$, $\alpha = 10 \text{ dB/MHz/cm}$. We evaluated the effect of decreasing the SNR, reducing signal separation (i.e., thinner samples), lowering the amplitude of the first signal (i.e., acoustic impedance contrast $|Z - Z_w|$), and increasing sample attenuation. Table I summarizes the ranges of all parameter values used in our simulations.

B. CRB approximation

In QAM simulations, i.i.d. zero-mean Gaussian noise with variance σ_x^2 is typically added in the time domain as described before. However, due to the division by Fourier coefficients during the transformation to the frequency domain, the noise no longer maintains its identical distribution. This discrepancy violates the assumptions made in Section IV for deriving the CRBs. To address this limitation, we consider an adjusted bound that approximates the power of the non-identically distributed noise with that of an identically distributed noise. Specifically, for each simulated signal, we extract the noise present in the truncated normalized spectrum and compute its sample variance. Then, the value of σ^2 used in Section IV is approximated by the average of these sample variances, calculated over a large number (e.g., 5,000) of simulated signals. Our experiments demonstrated that this practical adjustment still provides a reliable lower bound for studying the behavior of the estimators.

C. Ex vivo experiments

Experimental data were obtained using the 500 MHz QAM system described in [32] and collected from a 6- μm human lymph node section using a sampling frequency of 10 GHz. A 300-point RF signal was acquired at each spatial location using a 1- μm step size in both directions. An $60 \times 90 \mu\text{m}$ spatial region of interest (ROI) was selected for analysis.

D. Preprocessing

Before applying any estimation method, a Cadzow filter [33] is used to denoise the normalized spectrum \mathbf{x} . This process aims to reduce the rank of the Hankel matrix $H(\mathbf{x})$ to P .

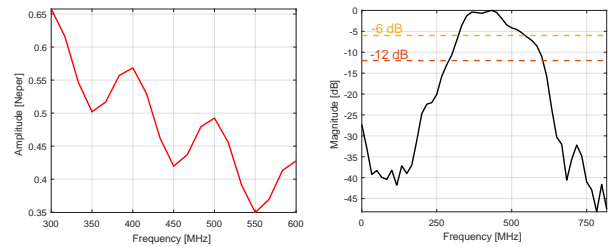


Fig. 2. Left: Illustration of the normalized spectrum (3) for a bandwidth limited at -12 dB. Right: Magnitude in dB of the reference signal to illustrate -12 dB and -6 dB bandwidths.

Specifically, the SVD of $H(\mathbf{x})$ is computed and $H(\mathbf{x})$ is then reconstructed by retaining only the P largest singular values. Then, a denoised version of \mathbf{x} is obtained by averaging all the anti-diagonals of the rank- P approximation of $H(\mathbf{x})$. This procedure is repeated five times [15].

In [19], we investigated whether this preprocessing step is essential for the non-weighted HK-based method. While its use was important in simulations, its impact on real data was minimal. Nonetheless, we continue to apply the Cadzow filter to ensure fairness when comparing performance with the AR-based method, which requires this denoising step.

The model order P can either be fixed (e.g., $P \geq 2$) or dynamically determined during the first iteration of the Cadzow filter, based on the number of singular values that contribute more than 10% to the total signal energy. This dynamic approach provides a more tailored representation of the underlying signal and is used for real data. For simulations, we set $P = 2$ because the CRB calculations depend on this value and the associated (known) spectral parameters.

The choice of bandwidth determines the range of frequencies where division in (3) is well-defined and affects the trade-off between the number of data points and the noise level in the truncated spectrum. The usable bandwidth typically includes frequencies within -6 to -12 dB of the center (or peak) frequency, depending on the sensitivity of the transducer and system technology, as obtained from \mathcal{F}_{h_0} [1]. Fig. 2 illustrates the normalized spectrum from (3) with a bandwidth limited at -12 dB, alongside the magnitude in dB of the reference signal (left plot), highlighting the -12 dB and -6 dB bandwidth limits. Unless otherwise stated, a -12 dB bandwidth is used for analysis. To better understand its impact, we investigate the effects of bandwidth selection on both simulations and real data.

VI. RESULTS

A. Simulations

Fig. 3 presents the estimation performance of the RHK (magenta solid line), HK (blue solid line), and AR (red solid line) estimators in simulated data, with variations in SNR, Z , d , α , and the selected bandwidth (rows 1 to 5, respectively). The root-mean-square error (RMSE) of the estimated acoustic parameters is compared to the square root of the approximated CRB (black dashed line). Each column corresponds to the estimation of c , Z , α , and d .

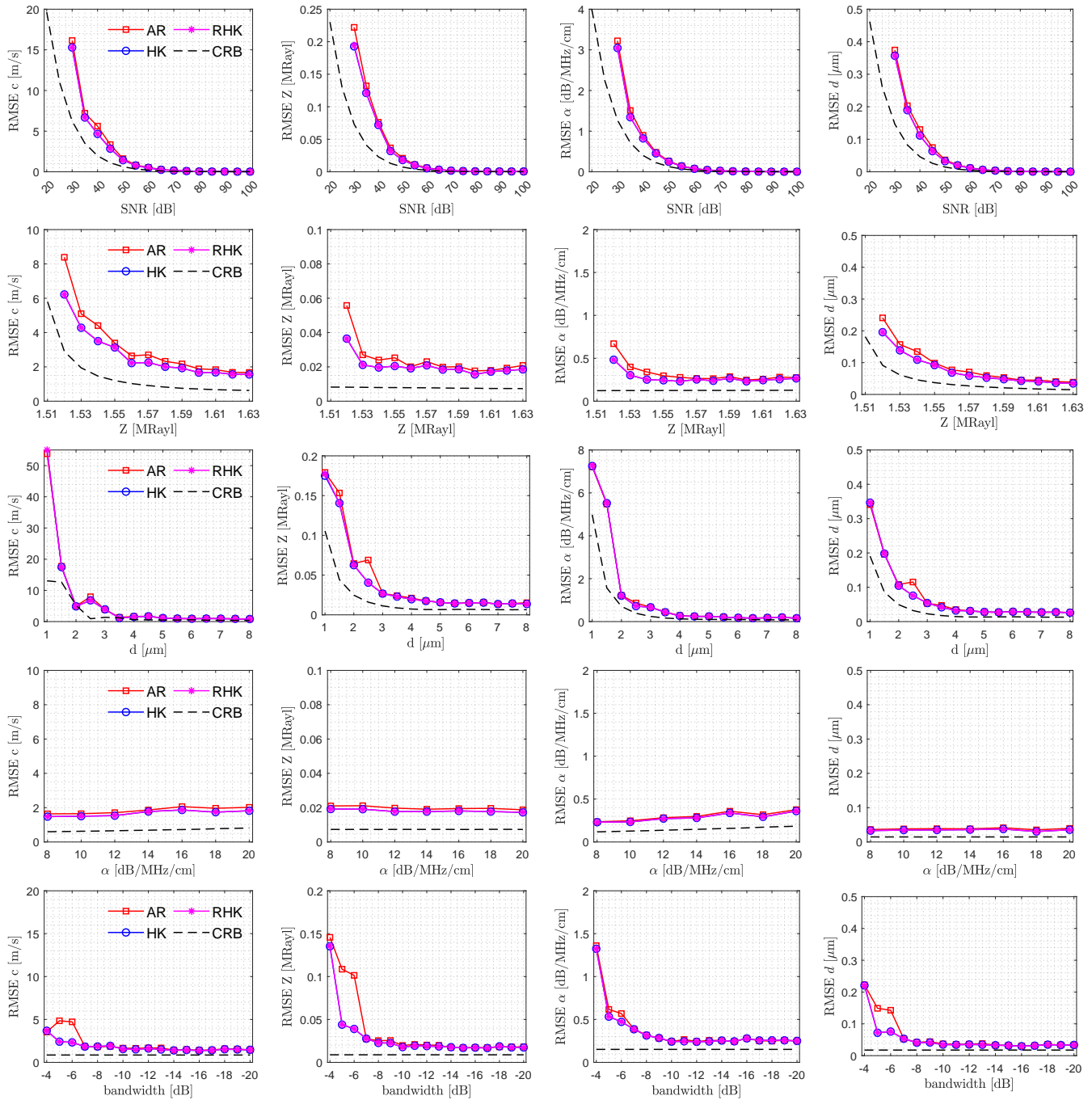


Fig. 3. Simulations results. Columns represent RMSE results (calculated after outlier removal) for c , Z , α and d . Rows show different parameter-set variations for SNR, Z , α and d . RHK is in magenta, HK is in blue, AR is in red, and the square root of the CRB is in black dashed line.

Outliers (estimates falling outside the established range) were identified and excluded from the RMSE calculation in cases where any method failed. Fig. 4 depicts the percentage of outliers detected for each method in each scenario, with RHK represented by magenta bars, HK by blue bars, and AR by red bars.

In Fig. 3 (top row), it can be observed that as SNR increases, both RMSE and CRB decrease for all parameters, as expected. At high SNR values (above 60 dB), noise has minimal impact, allowing all methods to approach the CRB. However, at lower SNR, the gap between RMSE and CRB becomes more noticeable, with HK-based methods exhibiting lower RMSE

values.

Fig. 4 (top left) shows that for SNRs below 50 dB, the number of outliers increases sharply for all methods. At SNR values of 20 dB, 25 dB and 30 dB, RHK demonstrated superior noise robustness, with reduced outlier rates of 84.5%, 66.5% and 47% respectively. In comparison, HK reported rates of 88.5%, 76.5% and 49.5% and AR produced significantly higher outlier rates of 99.5%, 98% and 76.5% at the same noise levels. The high proportion of outliers below 30 dB explains the absence of data points in the corresponding RMSE curves. At 35 dB and 40 dB, RHK and HK exhibited identical and reduced outlier rates of 22.5% and 3.5%, respectively,

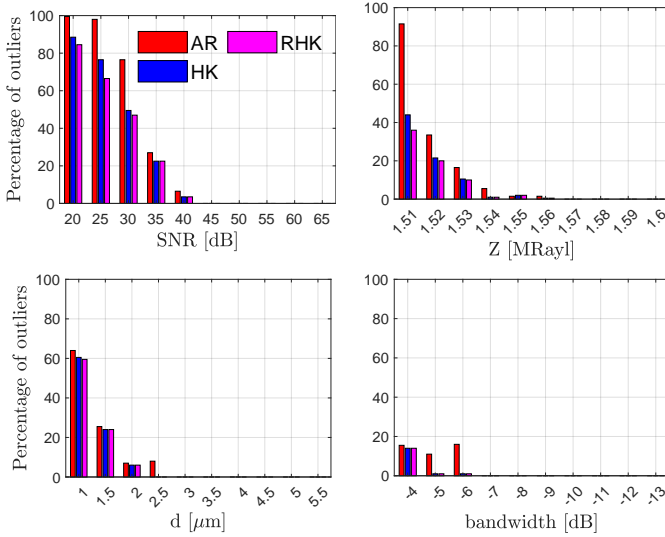


Fig. 4. Percentage of outliers detected for SNR, Z , d and bandwidth variation. RHK is represented in magenta, HK in blue and AR in red.

while AR reported higher rates of 27% and 6%.

Fig. 3 (second row) provides evidence that as Z decreases and approaches the impedance of water ($Z_w = 1.5$ MRayl), estimation becomes more challenging. This results in large RMSE values and a large gap relative to the CRB for all methods and parameters, which is expected because the amplitude of the water-tissue interface is proportional to $|Z - Z_w|$. However, this trend is not reflected in CRB_Z and CRB_α values, which remain almost constant. Moreover, HK-based methods achieve lower RMSE values and a reduced number of outliers compared to AR. In Fig. 4 (top right), AR shows significantly larger outlier rates of 91%, 33% and 16% at $Z = 1.51$, $Z = 1.52$, and $Z = 1.53$ MRayl, underscoring the improved robustness of HK-based methods in these scenarios. At the same Z values, RHK reported outlier rates of 36%, 20% and 10%, while HK presented outlier rates of 44%, 21% and 10.5%.

In Fig. 3 (third row), RMSE and CRB values decrease as d increases. For all estimators, the RMSE approaches the CRB for large d . This confirms that thicker samples yield more accurate parameter estimates, while thinner samples (small d) present greater challenges for reliable estimation. Overall, all methods achieve similar RMSE values, except at $d = 2.5 \mu\text{m}$, where HK-based methods demonstrate lower RMSE.

In terms of outliers (Fig. 4 bottom left), AR reported 64%, 25.5% and 7% for $d = 1$, $d = 1.5$ and $d = 2 \mu\text{m}$, respectively. HK-based methods showed reduced percentages at the same sample thicknesses: 60.5%, 24%, and 6% for HK and 59.5%, 24%, and 6% for RHK. For $d = 2.5 \mu\text{m}$, AR reported 8% outliers, while HK-based methods achieved zero outliers.

The fourth row of Fig. 3 demonstrates that as α increases, the RMSE slightly increases for the estimation of c and α . Notably, no outliers were detected in these experiments, thus the corresponding outliers report is omitted from Fig. 4.

The bottom row in Fig. 3 illustrates the impact of the bandwidth on the estimation performance. It is important to note that the CRB does not depend on the bandwidth,

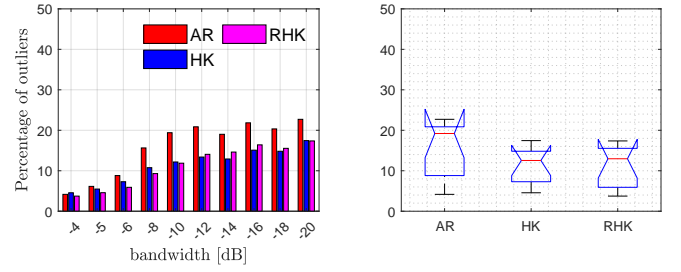


Fig. 5. Outlier report in real data ROI. Left: Percentage of outliers detected across bandwidth variations, with RHK represented in magenta, HK in blue, and AR in red. Right: Box plot illustrating the distribution of the percentage of outliers for each method.

remaining constant across all scenarios. However, the gap between the RMSE and the CRB becomes more pronounced when smaller bandwidths are used. This can be explained due to a smaller bandwidth reduces the number of frequencies available for analysis, resulting in less data and, consequently, a more challenging estimation. In these cases, HK-based methods exhibited better performance than AR, while from a bandwidth of -10 dB, the performance of all estimators stabilizes and remains asymptotically close to the CRB.

Outliers were observed only for bandwidths limited to -4 dB, -5 dB, and -6 dB, as shown in Fig. 4. HK and RHK exhibited a reduced number of outliers, reporting 14%, 1%, and 1%, respectively, compared to AR, which reported 15.5%, 11%, and 16% outliers under the same conditions. These results further validate the choice of a bandwidth of -12 dB as appropriate for achieving accurate parameter estimation in the simulated data.

To summarize, CRB curves play an important role, as expected, in predicting the behavior of the estimation algorithms and their dependence on parameter values and noise levels. Specifically, CRB_c depends on all parameters, while CRB_Z is influenced by Z and d . Additionally, CRB_α is dependent on all parameters except for Z , whereas CRB_d depends on all parameters except for α . Under favorable conditions, including high SNR, large Z and d , and low α , all methods show accurate performance with RMSE values approaching the CRB, demonstrating the reliability of the estimators. In challenging scenarios such as low SNR, small impedance contrasts, and thin samples, the proposed HK-based methods, particularly RHK, consistently outperform AR, achieving comparable or better estimation performance and significantly reducing the number of outliers.

B. Experiments

We conducted a study to evaluate the influence of bandwidth selection on the occurrence of unreliable estimates within the analyzed ROI. Fig. 5, on the left plot, presents the outlier ratios reported across different bandwidths, while on the right, box plots illustrate the distribution of the percentage of outliers for each method. All methods exhibited bandwidth dependency, with outlier ratios increasing as the bandwidth widened. This effect was more pronounced for the AR method compared to the HK methods. Interestingly, this behavior differs from the simulations, where a smaller number of data points was

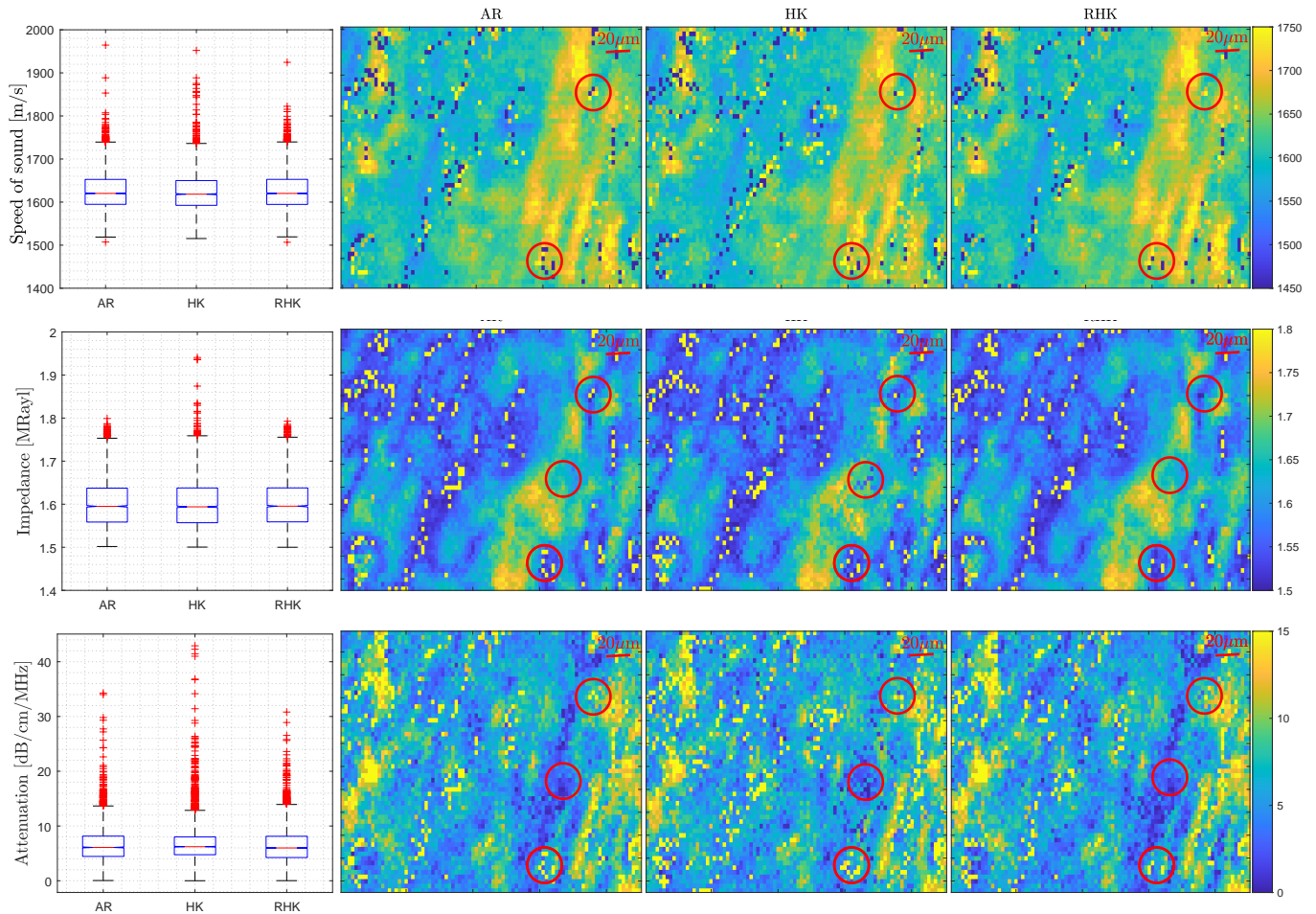


Fig. 6. Estimation results in real data ROI for a bandwidth at -4 dB (AR: 6%, HK: 5%, RHK: 4% outliers). Column 1: Box plot illustrating the distribution of parameter estimates after outlier removal for improved visualization. Columns 2-3: Results for AR, HK, and RHK methods. Rows 1-3: Correspond to c , Z and α , respectively.

expected to degrade performance. In the case of real data, the discrepancy can be explained by the inclusion of frequencies farther from the central frequency when larger bandwidths are used. These frequencies introduce non-stationary and additional noise sources, such as electronic noise, which are not captured by the current model.

Fig. 6 presents the estimation results for a bandwidth at -4 dB, which reported the lowest outlier rates across all methods (AR: 6%, HK: 5%, RHK: 4%). The first column displays box plots illustrating the distribution of parameter estimates after outlier removal for improved visualization. Columns 2 to 4 show the corresponding estimation maps without outlier removal for AR, HK, and RHK methods. The rows represent c , Z and α , respectively.

Pixels with small (dark blue) or large (intense yellow) unreliable values are more prevalent in AR and HK than RHK, consistent with their larger outlier rates. Regions highlighted by red circles illustrate the improvements offered by RHK.

For all parameters, the median (red line) and interquartile range (blue box width) are similar across all algorithms. Notably, RHK consistently produces narrower distributions compared to HK and AR, reflecting improved stability and robustness. This results in smoother maps, with significant differences observed, particularly for the estimation of α ,

where the RHK method demonstrates superior performance over its predecessor, HK.

To mitigate outliers, standard QAM post-processing image enhancement techniques can be applied to the estimated parameter maps. However, these techniques were omitted in this study to ensure a fair comparison between the different estimation frameworks.

VII. CONCLUSIONS AND PERSPECTIVES

In this work, we proposed a weighted HK-based framework for high-frequency signal processing in QAM. This method extends the baseline framework introduced in [19] by integrating a reweighting strategy based on redescending M-estimators. For the first time in the context of QAM, we derived CRBs, providing theoretical performance benchmarks for analyzing the accuracy of acoustic parameter estimation. Results in both simulated and experimental data at 500 MHz, demonstrated that the proposed approach consistently reduced outliers and improved parameter estimation accuracy compared to the standard AR approach, especially in challenging scenarios involving high noise levels or low impedance contrasts. These advancements come at a moderate computational cost, making the RHK framework a practical and effective alternative for real-world QAM applications.

Future work will seek to expand the scope and efficiency of the RHK framework. Testing datasets with varying noise levels and transducer frequencies, such as 1 GHz, will help identify scenarios where RHK surpasses HK, facilitating adaptive applications in more demanding conditions. Reducing the computational complexity of HK-based methods will be a key focus, with techniques like low-rank matrix factorization [34] offering promising solutions for scalability and real-time processing. Additional research will explore strategies to enhance robustness against variations in model order and bandwidth selection, as well as the integration of spatial information for joint or multivariate analyses to increase the flexibility of HK-based approaches. Finally, adopting deep unfolding methods [35] could improve optimization processes and robustness, paving the way for further advancements in this field.

VIII. COMPLIANCE WITH ETHICAL STANDARDS

The protocol (22-06024887) was approved by Weill Cornell Medicine Institutional Review board on August 2, 2023.

IX. ACKNOWLEDGMENTS

We are grateful to the authors of [18] who have kindly provided us with the original code of their paper.

REFERENCES

- [1] C. Hoerig and J. Mamou, *Advanced Topics in Quantitative Acoustic Microscopy*. Springer International Publishing, 2023, pp. 253–277.
- [2] R. A. Lemons and C. F. Quate, “Acoustic microscopy: Biomedical applications,” *Science*, vol. 188, no. 4191, pp. 905–911, 1975.
- [3] J. A. Hildebrand, D. Rugar, R. N. Johnston, and C. F. Quate, “Acoustic microscopy of living cells,” *Proceedings of the National Academy of Sciences*, vol. 78, no. 3, pp. 1656–1660, 1981.
- [4] D. Rohrbach, R. H. Silverman, D. Chun, H. O. Lloyd, R. Urs, and J. Mamou, “Improved high-frequency ultrasound corneal biometric accuracy by micrometer-resolution acoustic-property maps of the cornea,” *Transl. Vis. Sci. Technol.*, vol. 7, no. 2, p. 21, 2018.
- [5] M. F. Marmor, H. K. Wickramasinghe, and R. A. Lemons, “Acoustic microscopy of the human retina and pigment epithelium,” *Investigative Ophthalmology & Visual Science*, vol. 16, no. 7, pp. 660–666, 1977.
- [6] D. Rohrbach, H. O. Lloyd, R. H. Silverman, and J. Mamou, “Fine-resolution maps of acoustic properties at 250 MHz of unstained fixed murine retinal layers,” *The Journal of the Acoustical Society of America*, vol. 137, no. 5, p. EL381–EL387, 2015.
- [7] S. Irie, K. Inoue, K. Yoshida, J. Mamou, K. Kobayashi, H. Maruyama, and T. Yamaguchi, “Speed of sound in diseased liver observed by scanning acoustic microscopy with 80 MHz and 250 MHz,” *The Journal of the Acoustical Society of America*, vol. 139, no. 1, pp. 512–519, 2016.
- [8] A. K. Lawton, T. Engstrom, D. Rohrbach, M. Omura, D. H. Turnbull, J. Mamou, T. Zhang, J. M. Schwarz, and A. L. Joyner, “Cerebellar folding is initiated by mechanical constraints on a fluid-like layer without a cellular pre-pattern,” *eLife*, vol. 8, p. e45019, 2019.
- [9] D. Rohrbach, Q. V. Hoang, Q. Wen, S. A. McFadden, R. H. Silverman, and J. Mamou, “Fine-resolution elastic-property maps of myopic sclera by means of acoustic microscopy,” in *2015 IEEE International Ultrasonics Symposium (IUS)*, 2015, pp. 1–4.
- [10] Q. V. Hoang, D. Rohrbach, S. A. McFadden, and J. Mamou, “Regional changes in the elastic properties of myopic guinea pig sclera,” *Experimental Eye Research*, vol. 186, p. 107739, 2019.
- [11] J. Mamou, D. Rohrbach, E. Saegusa-Beecroft, E. Yanagihara, J. Machi, and E. J. Feleppa, “Ultrasound-scattering models based on quantitative acoustic microscopy of fresh samples and unstained fixed sections from cancerous human lymph nodes,” in *2015 IEEE International Ultrasonics Symposium (IUS)*, 2015, pp. 1–4.
- [12] G. A. D. Briggs, J. Wang, and R. Gungl, “Quantitative acoustic microscopy of individual living human cells,” *Journal of Microscopy*, vol. 172, no. 1, pp. 3–12, 1993.
- [13] E. C. Weiss, P. Anastasiadis, G. Pilarczyk, R. M. Lemor, and P. V. Zinin, “Mechanical properties of single cells by high-frequency time-resolved acoustic microscopy,” *IEEE Transactions on Ultrasonics, Ferroelectrics, and Frequency Control*, vol. 54, no. 11, pp. 2257–2271, 2007.
- [14] N. Hozumi, R. Yamashita, C.-K. Lee, M. Nagao, K. Kobayashi, Y. Saijo, M. Tanaka, N. Tanaka, and S. Ohtsuki, “Time–frequency analysis for pulse driven ultrasonic microscopy for biological tissue characterization,” *Ultrasonics*, vol. 42, no. 1-9, pp. 717–722, 2004.
- [15] D. Rohrbach and J. Mamou, “Autoregressive signal processing applied to high-frequency acoustic microscopy of soft tissues,” *IEEE Transactions on Ultrasonics, Ferroelectrics, and Frequency Control*, pp. 1–1, 2018.
- [16] G. R. Prony, “On the analysis of spectral lines by the method of least squares,” *Royal Society of London Philosophical Transactions Series I*, vol. 85, pp. 373–518, 1795.
- [17] K.-H. Jin, J.-C. Um, D.-H. Lee, J. Lee, S.-W. Park, and J.-C. Ye, “MRI artifact correction using sparse + low-rank decomposition of annihilating filter-based Hankel matrix,” *Magnetic Resonance in Medicine*, vol. 78, no. 1, pp. 327–340, 2017.
- [18] F. Andersson, M. Carlsson, J.-Y. Tourneret, and H. Wendt, “A new frequency estimation method for equally and unequally spaced data,” *IEEE T. Signal Proces.*, vol. 62, no. 21, pp. 5761–5774, 2014.
- [19] L. Leon, J. Mamou, D. Kouamé, and A. Basarab, “Hankel-based spectral method for quantitative acoustic microscopy,” in *2024 IEEE International Symposium on Biomedical Imaging (ISBI)*, 2024, pp. 1–5.
- [20] P. Stoica and R. Moses, *Spectral Analysis of Signals*. Pearson Prentice Hall, 2005.
- [21] R. Rochberg, “Toeplitz and Hankel operators on the Paley-Wiener space,” *Integral Equations and Operator Theory*, vol. 10, no. 2, pp. 187–235, 1987.
- [22] F. Andersson, M. Carlsson, and M. V. de Hoop, “Sparse approximation of functions using sums of exponentials and AAK theory,” *Journal of Approximation Theory*, vol. 163, no. 2, pp. 213–248, 2011.
- [23] S. Boyd, N. Parikh, E. Chu, B. Peleato, and J. Eckstein, *Distributed Optimization and Statistical Learning via the Alternating Direction Method of Multipliers*, 2011.
- [24] R. Roy and T. Kailath, “ESPRIT-estimation of signal parameters via rotational invariance techniques,” *IEEE Transactions on Acoustics, Speech, and Signal Processing*, vol. 37, no. 7, pp. 984–995, 1989.
- [25] A. E. Beaton and J. W. Tukey, “The fitting of power series, meaning polynomials, illustrated on band-spectroscopic data,” *Technometrics*, vol. 16, no. 2, pp. 147–185, 1974.
- [26] N. Ouzir, A. Basarab, O. Lairez, and J.-Y. Tourneret, “Robust optical flow estimation in cardiac ultrasound images using a sparse representation,” *IEEE Transactions on Medical Imaging*, vol. 38, no. 3, pp. 741–752, 2019.
- [27] P. Meer, D. Mintz, A. Rosenfeld, and D. Y. Kim, “Robust regression methods for computer vision: A review,” *International Journal of Computer Vision*, vol. 6, no. 1, p. 59–70, 1991.
- [28] J. Odobez and P. Bouthemy, “Robust multiresolution estimation of parametric motion models,” *Journal of Visual Communication and Image Representation*, vol. 6, no. 4, pp. 348–365, 1995.
- [29] H. L. V. Trees, *Detection, Estimation, and Modulation Theory, Part I*. John Wiley & Sons, Inc., 2001.
- [30] E. Gudmundson, P. Wirfalt, A. Jakobsson, and M. Jansson, “An Esprit-based parameter estimator for spectroscopic data,” in *2012 IEEE Statistical Signal Processing Workshop (SSP)*. IEEE, 2012.
- [31] Y.-X. Yao and S. Pandit, “Cramer-Rao lower bounds for a damped sinusoidal process,” *IEEE Transactions on Signal Processing*, vol. 43, no. 4, p. 878–885, 1995.
- [32] D. Rohrbach, A. Jakob, H. O. Lloyd, S. H. Tretbar, R. H. Silverman, and J. Mamou, “A novel quantitative 500-MHz acoustic microscopy system for ophthalmologic tissues,” *IEEE Transactions on Biomedical Engineering*, vol. 64, no. 3, pp. 715–724, 2017.
- [33] J. Cadzow, “Signal enhancement—a composite property mapping algorithm,” *IEEE Transactions on Acoustics, Speech, and Signal Processing*, vol. 36, no. 1, pp. 49–62, 1988.
- [34] D. Guo, H. Lu, and X. Qu, “A fast low rank hankel matrix factorization reconstruction method for non-uniformly sampled magnetic resonance spectroscopy,” *IEEE Access*, vol. 5, pp. 16 033–16 039, 2017.
- [35] Y. Huang, J. Zhao, Z. Wang, V. Orekhov, D. Guo, and X. Qu, “Exponential signal reconstruction with deep hankel matrix factorization,” *IEEE Transactions on Neural Networks and Learning Systems*, vol. 34, no. 9, pp. 6214–6226, 2023.